Chiral cation doping for modulating structural symmetry of 2D perovskites

Yi Xie,^{1,2} Jack Morgenstein,¹ Benjamin G. Bobay,³ Ruyi Song,⁴ Naidel A. M. S. Caturello,⁵ Peter C. Sercel,⁶ Volker Blum^{1,4} and David B. Mitzi^{1,4}*

¹Thomas Lord Department of Mechanical Engineering and Materials Science, Duke University, Durham, NC 27708, USA.

²University Program in Materials Science and Engineering, Duke University, Durham, NC 27708, USA.

³Duke University NMR Center, Duke University Medical Center, Durham, NC 27710, USA.

⁴Department of Chemistry, Duke University, Durham, NC 27708, USA.

⁵ Federal University of ABC, 09210-580, Santo André, São Paulo, Brazil.

⁶Center for Hybrid Organic Inorganic Semiconductors for Energy, Golden, CO 80401, USA.

*e-mail: david.mitzi@duke.edu

Keywords: Perovskites, Cation mixing, Symmetry breaking, Spin splitting, Circular dichroism

Abstract

Cation-mixing in two-dimensional (2D) hybrid organic-inorganic perovskite (HOIP) structures represents an important degree of freedom for modifying organic templating effects and tailoring inorganic structures. However, the limited number of known cation-mixed 2D HOIP systems generally employ a 1:1 cation ratio for stabilizing the 2D perovskite structure. Here, we demonstrate a chiral-chiral mixed-cation system wherein a controlled small amount (<10 %) of chiral cation S-2-MeBA (S-2-MeBA = (S)-(-)-2-methylbutylammonium) can be doped into (S- $BrMBA)_2PbI_4$ (S-BrMBA = (S)-(-)-4-bromo-\alpha-methylbenzylammonium), modulating the structural symmetry from a higher symmetry (C2) to the lowest symmetry state (P1). This structural change occurs when the concentration of S-2-MeBA, measured by solution nuclear magnetic resonance, exceeds a critical level—specifically, for 1.4 ± 0.6 %, the structure remains as C2, whereas 3.9 ± 1.4 % substitution induces the structure change to P1 (this structure is stable to \sim 7% substitution). Atomic occupancy analysis suggests that one specific S-BrMBA cation site is preferentially substituted by S-2-MeBA in the unit cell. Density-functional theory calculations indicate that the spin splitting along different k-paths can be modulated by cation doping. A true circular dichroism band at the exciton energy of the 3.9% doping phase shows polarity inversion and a ~45 meV blue shift of the Cotton-effect-type line-shape relative to (S-BrMBA)₂PbI₄. A trend toward suppressed melting temperature with higher doping concentration is also noted. The chiral cation doping system and the associated doping-concentration-induced structural transition provide a material design strategy for modulating and enhancing those emergent properties that are sensitive to different types of symmetry breaking.

Introduction

Two-dimensional hybrid organic-inorganic perovskite (HOIP) semiconductors exhibit compositional and structural versatility owing to the broad flexibility afforded by substituting organic and inorganic components. 1-5 As a result, a variety of physical properties, particularly those sensitive to the detailed perovskite structure, can be modulated and enhanced, such as energy harvesting, 2-3 light-emission, 6-7 ferroelectricity, 8-9 and spin character of energy bands and optical response, with possible applications in fields ranging from optoelectronics to spintronics. 10-14 While a wide range of single cations has been incorporated into the 2D HOIP framework, cation mixing on the organic sites has been demonstrated as an extra degree of freedom for stabilizing layered perovskite structures with different structural characteristics. 15-17 Mitzi et al. 15 reported a 1:1 ratio cation-mixed 2D HOIP system, (5FPEA)(NEA)SnI₄ (5FPEA = 2,3,4,5,6pentafluorophenethylammonium, NEA = 2-naphthyleneethylammonium), wherein uniform cation layers of 5FPEA and NEA alternate along the stacking direction and fluoroaryl-aryl interactions stabilize the structures. Subsequently, a series of mixed-cation systems with an alternating arrangement of two types of cations within individual organic layers were explored. 16-17 Compared with single-cation organic structures, cation mixing offers additional advantages of flexible combinations of distinct structure-directing characteristics, such as the above mentioned fluoroaryl-aryl mixing, 15 alkyl – aryl mixing in $(BA_{0.5}PEA_{0.5})_2MAPb_2Br_7$ (BA = butylammonium;PEA = phenethylammonium; MA = methylammonium)¹⁷ and chiral-achiral mixing in (S-MePEA)(C3A)PbBr₄ (S-MePEA = S- β -methylphenethylammonium; C3A = propylammonium) and (S-MePEA)(C4A)PbBr₄ (C4A = butylammonium). ¹⁶ Notably, the ratio between the two types of cations in these systems is generally reported as and limited to approximately 1:1. Often there are compelling structural reasons for this specific ratio—i.e., the 1:1 cation-mixed phase can be stabilized by the enhanced noncovalent interaction between the distinct and alternating layers of the fluoroaryl and aryl cations in the fluoroaryl-aryl mixed system¹⁵ or between the alkyl and aryl cations that pack alternatingly in an ordered fashion within the single layer in the alkyl-aryl mixed system¹⁶. Nevertheless, exploring cation mixing ratios beyond 1:1 may offer important opportunities to further enhance the range of distortions and possibly allow for further breaking of structural symmetries in the 2D HOIPs, if structural paradigms can be identified that allow for such flexibility in the organic cation stoichiometry.

Given such tunable templating effects of the organic cations, mediated by complex hydrogen bonding contacts between the ammonium groups of these cations and the halogens in the metal halide perovskite sheets, we hypothesize that the pristine (single cation) structural symmetry may be broken by distorting the atomic arrangements from their original symmetric positions if more general cation mixing ratios can be achieved. As a result, structural symmetry elements can be annihilated, leading to structural change from a higher-symmetry state to a lowsymmetry state. The diverse symmetry elements, such as inversion, mirror, rotational, and timereversal symmetries that can be broken in 2D HOIP structures enable the integration of different degrees of structural distortions and lattice symmetries into the HOIP family. In solid state physics, many phenomena are known to be unique to specific types of symmetry breaking. For instance, inversion symmetry breaking can lead to Rashba/Dresselhaus spin splitting, 18-20 even-order nonlinear effects,²¹ and Ising superconductivity.²²⁻²³ In contrast, rotational symmetry breaking can induce the bulk photovoltaic effect,²⁴ nonlinear Hall effect,²⁵ and valley magnetoelectricity.²⁶ Thus, the ability to implement different types of symmetry in crystalline structures is an essential tool to control and enhance specific physical properties of interest.²¹ Although the inversion symmetry of the inorganic framework has been broken to a significant degree in some 2D HOIP systems via chirality transfer, ²⁷⁻²⁸ the typical space groups associated with the isolated inorganic layers, such as $P2_1$, $P2_12_12_1$, and $Pmc2_1$, indicate that some symmetry elements (i.e., screw axis, mirror plane, and glide plane) remain preserved. The restricted degree of distortions induced by these chiral cations poses limitations for further enhancing chirality transfer and tailoring the inorganic sublattice to a lower symmetry state.

Here, we demonstrate that the structural symmetry of 2D HOIPs can be modulated from a higher symmetry (C2) to the lowest symmetry (P1) state by doping the chiral 2D HOIP system (S-BrMBA)₂PbI₄ (S-BrMBA = (S)-(-)-4-bromo- α -methylbenzylammonium) with a small amount (< 5%) of chiral (S)-(-)-2-methylbutylammonium (S-2-MeBA) (Supplementary Figure 1), wherein the organic layer is rearranged and an additional degree of distortion is induced to break C_2 rotational symmetry. Single crystal X-ray diffraction investigation indicates that such doping-induced crystal manipulation and symmetry breaking can only be achieved when incorporating a critical amount of dopant (S-2-MeBA) into the host system. A lower doping concentration (i.e., 1.4 ± 0.6 %) leaves the global system in the original structure with negligible structural change,

while a higher concentration (i.e., $3.9 \pm 1.4\%$) induces the transition. The cation substitution is found to occur preferentially on one of the four distinct S-BrMBA cation sites within the unit cell and is likely facilitated by the favorable relative position of the ammonium group of the specific S-BrMBA cation. The doping concentrations were experimentally verified using solution nuclear magnetic resonance (NMR), pointing to good agreement with the values of chemical occupancy determined by single crystal X-ray diffraction. Our work opens a new pathway to stabilize a mixedcation system with a mixing ratio other than 1:1 and achieves a controlled doping-concentrationdependent structural transition, leading to an altered chirality transfer to and symmetry breaking in the inorganic layer. Density-functional theory (DFT) calculations show split bands along different k-paths that are known to be associated with spin splitting due to inversion symmetry breaking in layered perovskites, and the magnitude of the splitting can be modulated due to doping with S-2-MeBA. The circular dichroism (CD) band at the exciton transition of the 3.9% doping phase exhibits polarity inversion and blue-shifts by ~45 meV relative to that in (S-BrMBA)₂PbI₄, while the linear absorption exciton transition energy is not shifted; moreover, the CD is demonstrated to be intrinsic. Finally, differential scanning calorimetry (DSC) characterization indicates that a higher doping concentration leads to a lower melting temperature and points to the potential for suppressing the melting temperature of 2D HOIPs via cation doping for future film, crystal or monolith melt processing. We believe the new approaches provided by this study will benefit future material researchers who are interested in exploring a wider range of 2D perovskite systems with exceptional structural and symmetry-related properties.

Results and Discussion

Chiral cation doping to induce the structural transition. The steric effects associated with the spatial arrangement and conformation of the organic cations directly impact the structural distortions and symmetries of the inorganic sublattice.²⁹ Incorporating diverse functional groups into the organic cations can be one avenue to enhance the steric hindrance^{5, 29-30}. In this context, S-BrMBA, comprising rigid benzene, bromine substitution, and chirality (Supplementary Figure 1a), was selected and predicted to be able to stabilize a strained structure with enlarged distortions and lower symmetry. To explore the structural characteristics templated by this cation, single-crystal X-ray diffraction (SC-XRD) was performed to characterize the crystal structure of (S-BrMBA)₂PbI₄ (Supplementary Table 1). The compound crystallizes as a Ruddlesden–Popper type

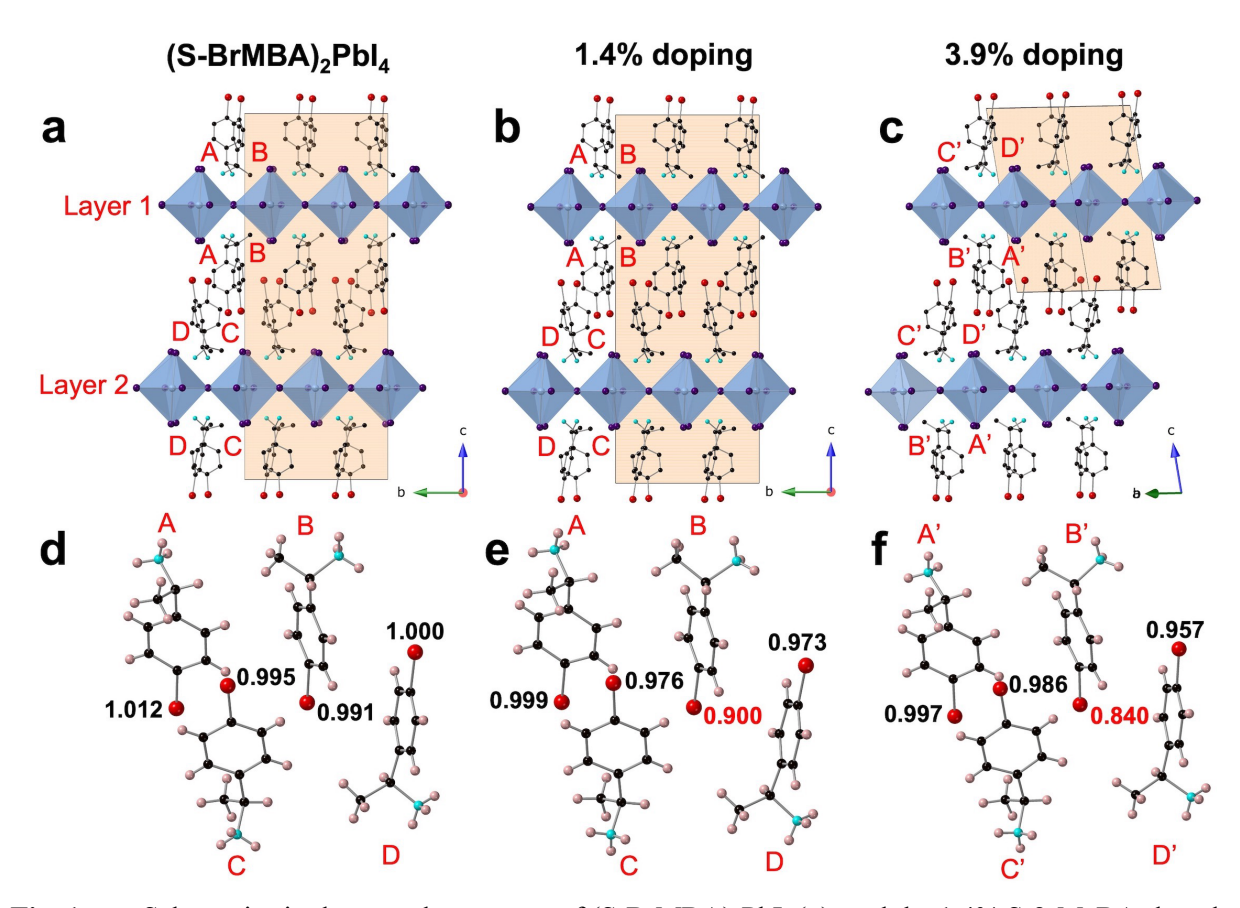


Fig. 1: a-c Schematic single-crystal structures of (S-BrMBA)₂PbI₄ (**a**), and the 1.4% S-2-MeBA-doped (**b**) and 3.9% S-2-MeBA-doped (**c**) variants. Unit cells in a-c are indicated by shaded parallelograms. Four types of chiral cations are labeled as A, B, C, and D for undoped (S-BrMBA)₂PbI₄ and for the 1.4% doped structure, versus A', B', C', and D' for the 3.9% S-2-MeBA doped structure. **d-f**, Conformation of chiral organic cations and chemical occupancy of Br atoms corresponding to the structures (**a-c**). Chemical occupancy values in red point to cations that are preferentially substituted by S-2-MeBA. Blue, purple, red, black, turquoise, and beige spheres denote Pb, I, Br, C, N, and H atoms, respectively.

structure, with bilayers of well-ordered organic cations intercalated between 2D inorganic layers of corner-sharing PbI₆ octahedra (Figure 1a). Reflecting the incorporation of the chiral cation, (S-BrMBA)₂PbI₄ crystallizes in a non-centrosymmetric *C*2 space group. To study the inorganic structural symmetry, PLATON analysis was performed for the isolated inorganic sublattice (after removing the organic cations from the structure³¹; see Methods), which points to a nominally centrosymmetric *C*2/*c* space group (using the default positional/angular tolerance criteria, i.e., 0.3°, 0.25 Å, 0.25 Å). Notably, there are two different inorganic layers (designated as layer 1 and layer 2; see Figure 1a) contained in the unit cell. The symmetry of the individual inorganic

layers is determined to be C2 for layer 1 and C2/m for layer 2 (Supplementary Table 2). As shown in Figure 1a, there are four types of S-BrMBA cations with different conformations in the unit cell. Type A and B cations are alternatingly arranged within the same organic layers and interact with inorganic layer 1 via hydrogen (H) bonding interactions. Correspondingly, type C and D cations are arranged in a similar fashion in the remaining organic layers and bond to inorganic layer 2. The relatively different steric effects of the two subgroups (A, B vs. C, D) of S-BrMBA cations result in the two inorganic layers (layers 1 and 2) with distinct structural characteristics.

To investigate the impact of the individual functional groups contained in S-BrMBA on inorganic structural symmetry and distortions, the global vs. inorganic space groups and distortion parameters of several 2D HOIP systems templated by aromatic cations, including (BzA)₂PbI₄,³⁰ (S-MBA)₂PbI₄,²⁷ (4-BrBzA)₂PbI₄,³⁰ and the presently investigated (S-BrMBA)₂PbI₄, with different selections of functional groups (i.e., benzene, bromine substitution, and chirality) are analyzed and listed in Table 1. The inorganic structural distortions are quantified by a list of indicators. The equatorial Pb-I-Pb bond angle β is used to evaluate the inter-octahedral distortion. The bond length distortion, $\Delta d = \left(\frac{1}{6}\right) \Sigma (d_i - d_0)^2 / {d_0}^2$ (d_i are the six Pb-I bond lengths and d_0 is the mean Pb-I bond length within a PbI₆ octahedron), and bond angle variance, σ^2 = $\Sigma_{i=1}^{12}(\theta_i-90)^2/11$ (θ_i are the twelve I-Pb-I bond angles within a PbI₆ octahedron),³² are used to evaluate the intra-octahedral distortion. Compared to (S-MBA)₂PbI₄, additional bromine substitution in S-BrMBA leads to a relatively lower structural symmetry (C2 vs. P2₁2₁2₁) and larger inter-octahedral distortion, revealed by the smaller bond angle θ that deviates more from the ideal 180°. Compared with (4-BrBzA)₂PbI₄, although the structural symmetries are comparable (C2 vs. P2₁), the chirality included in (S-BrMBA)₂PbI₄ results in larger inter- and intra-octahedral distortions. Thus, this analysis suggests a possible strategy that incorporating chirality and bromine substitution into the organic cation (i.e., S-BrMBA) may enlarge the steric hindrance and enhance the structural distortion and symmetry breaking within the inorganic sublattice. Additionally, we also used tighter tolerance criteria, i.e., 0.2°, 0.05 Å, 0.05 Å, 0.05 Å, to analyze the space group symmetries for this array of 2D HOIP systems (Supplementary Table 3) and find that the space group for the global structure is unchanged; however, the glide plane symmetries within the inorganic layers of (S-MBA)₂PbI₄, (4-BrBzA)₂PbI₄, and (S-BrMBA)₂PbI₄ are missing, indicating the impact of the tolerance criteria on the detection of symmetry elements (i.e., that comparisons

need to be made at a consistent level of tolerance factors). Note that C_2 rotational symmetry remains in (S-BrMBA)₂PbI₄, leading to the interesting question of whether we can further modulate the structure to adopt an even lower symmetry state.

Table 1. Summary of global vs. inorganic layer space group symmetries and distortion parameters for several previously reported 2D HOIP systems (references given), as well as for the presently reported (S-BrMBA)₂PbI₄-related systems. (Default positional/angular tolerance criteria, i.e., 0.3°, 0.25 Å, 0.25 Å, 0.25 Å, are used in PLATON, which can only approximate the structural symmetries.)

Compound	Cation	Global	Inorganic (Individual inorganic layer)	Δd (10^{-4})	σ^2 (°2)	θ (°) [Δθ]
(BzA) ₂ PbI ₄ ³⁰	NH ₂	Pbca	Pbca	0.07	11.88	157.80, 157.80 [0]
(S-MBA) ₂ PbI ₄ ²⁷	NH ₂	P2 ₁ 2 ₁ 2 ₁	Pnma	5.64	20.11	151.45, 157.30 [5.85]
(4-BrBzA) ₂ PbI ₄ ³⁰	Br NH ₂	P2 ₁	P2 ₁ /c	0.86	8.39	155.54, 152.50 [3.04]
(S-BrMBA) ₂ PbI ₄	NH ₂ CH ₃	C2	C2/c (C2, C2/m)	7.71, 2.49	13.67, 12.02	154.26, 156.40, 147.87, 156.40 [8.53] 148.71, 152.86, 157.02, 152.86 [8.31]
(S-2-MeBA) _x (S-BrMBA) _{2-x} PbI ₄ (3.9%)	Br + H ₃ C NH ₂ CH ₃	<i>P</i> 1	<i>P</i> 1	3.86, 2.39	14.47, 9.93	148.90, 154.12, 154.97, 154.75 [6.07]

We therefore targeted doping a small amount of chiral organic cation S-2-MeBA into (S-BrMBA)₂PbI₄, with the goal of introducing heterogeneity into the chiral organic layer. This heterogeneity might be expected to disturb the cation arrangement and break the symmetry within this layer and, through asymmetric steric and hydrogen bonding interactions, perhaps impact the inorganic sublattice as well. Initial attempts at mixing the organic cations during solution-phase synthesis (see Methods) led to a product (labeled as "3.9% doping") that adopts a triclinic *P*1 rather

than monoclinic *C*2 (as for (S-BrMBA)₂PbI₄) crystal system (Supplementary Table 1). We observe different crystal morphology between the two phases (Supplementary Figure 2). (S-BrMBA)₂PbI₄ shows uniformly shaped cubic crystals, while the S-2-MeBA "3.9% doping" material shows less uniform and smaller plate-shape crystals. Notably, as we decrease the doping concentration by tuning the ratio between the two organic cations in the precursor solution during crystal growth (see Methods), the structural transition is absent in the lower-dopant-concentration material (labeled as "1.4% doping"), although the associated lattice parameters are slightly smaller than those of (S-BrMBA)₂PbI₄ (Supplementary Table 1) owing to the smaller volume occupied by S-2-MeBA relative to S-BrMBA. Thus, the observed global structural transition is doping-concentration-dependent and cannot be induced until the doping concentration reaches a critical value.

To quantify/verify the doping concentration that dictates this structural transition (and to justify the naming convention for the doped systems), we performed solution NMR characterization for the samples with different doping levels. ¹H NMR spectra were collected for the dissolved single cation materials (S-2-MeBA)₂PbI₄ and (S-BrMBA)₂PbI₄ individually at first (Supplementary Figure 3) for reference, to determine the degree of spectral overlap, and unambiguously identify which peaks can be used for quantification (Figure 2a). One peak from the S-BrMBA cation is particularly isolated from the rest of the peaks (the quartet—i.e., a single hydrogen peak that is split into 4 peaks, as it is immediately adjacent to a CH₃ group—at ~4.5 ppm, representing the CH group of the molecule) and affords the opportunity to quantify the level of S-2-MeBA cation incorporation utilizing peaks at approximately 2.7, 2.6, 1.6, 0.9, and 0.8 ppm for the latter cation. Integrating these peaks with respect to the peak at 4.5 ppm and accounting for the number of hydrogens that each peak represents results in a measured value of $1.4 \pm 0.6\%$ incorporation of S-2-MeBA cation in the relatively lower doping concentration sample ((S-2-MeBA)_{0.028}(S-BrMBA)_{1.972}PbI₄) and 3.9 \pm 1.4% of S-2-MeBA cation in the relatively higher doping concentration sample ((S-2-MeBA)_{0.078}(S-BrMBA)_{1.922}PbI₄) (Figure 2b-c). In the following, in accordance with the above results (which will be further validated by crystal structure refinement, as described below), we designate these two structures as "1.4% doping" and "3.9% doping", respectively.

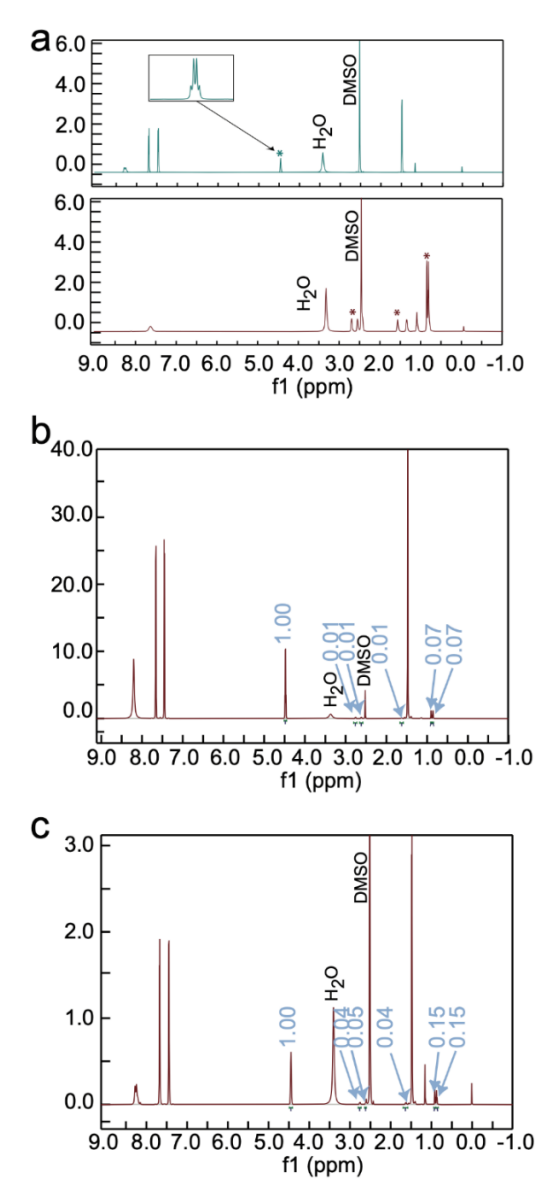


Fig. 2: a-c ¹H NMR spectra of **(a)** S-2-MeBA (maroon) and S-BrMBA (cyan) cations by dissolving single-cation (S-2-MeBA)₂PbI₄ and (S-BrMBA)₂PbI₄ in DMSO, **(b)** relatively low concentration S-2-MeBA doping sample $(1.4 \pm 0.6\%)$ ((S-2-MeBA)_{0.028}(S-BrMBA)_{1.972}PbI₄ crystal), and **(c)** relatively high concentration S-2-MeBA doping sample $(3.9 \pm 1.4\%)$ ((S-2-MeBA)_{0.078}(S-BrMBA)_{1.922}PbI₄ crystal). Integration values noted in blue and * denote signals used for analysis.

SC-XRD characterizations for the 1.4% and 3.9% doping materials were performed to investigate the impact of different degrees of S-2-MeBA doping on the structural characteristics (structural difference relative to (S-BrMBA)₂PbI₄) and to gain further insight into the positioning and occupancies associated with the S-2-MeBA dopant. In the x-ray crystallographic structures, instead of assuming that the chemical occupancy of each atom is 1 (full occupancy) during the

process of structure refinement, we initially freed the chemical occupancies of Pb, I, and Br atoms in the three structures for assessing the actual occupancies based on the SC-XRD data. The observed occupancies of essentially 1 (to within ± 0.04) for Pb and I atoms (Supplementary Table 4) indicate that these sites are fully occupied, independent of the doping in the organic layer. Considering that Br is not contained in the dopant S-2-MeBA, the chemical occupancy of Br can directly reflect the incorporation of the dopant S-2-MeBA relative to the host cation S-BrMBA. As shown in Figure 1d-f and Supplementary Table 4, the chemical occupancies of the four types of Br atoms in (S-BrMBA)₂PbI₄ are shown to be 1.012 (type A), 0.991 (type B), 0.995 (type C), and 1.000 (type D), which are all near full occupancy. In the 1.4% doping structure, the chemical occupancy of one specific type of Br atom (0.900, belonging to type B S-BrMBA) is significantly lower than the other three types of Br atoms (0.999, 0.976, 0.973), which points to the possibility that type B S-BrMBA is partially substituted by S-2-MeBA. As the doping concentration increases to 3.9% and a structural transition is induced, the chemical occupancy of the corresponding type B' Br atom further decreases to 0.840, corresponding to the higher proportion of S-2-MeBA dopant on this site. The chemical occupancies of the other three Br atoms in the 3.9% doping structure are similar to those of the (S-BrMBA)₂PbI₄ and 1.4% doping structures. To validate that the doping induced structural transition is due to the doping of S-2-MeBA, and not to a simple vacancy on this cation site, a reference precursor solution with the same recipe as for the 3.9% doping sample, except for removing the dopant S-2-MeBA, was prepared. The as-synthesized crystals (Supplementary Table 5) show the same structure type and similar lattice constants as (S-BrMBA)₂PbI₄, indicating that the structural transition cannot occur without substituted S-2-MeBA. In addition, the occupancy of 0.840 determined for the type B' Br in the 3.9% doping structure corresponds to a ~0.16 substitution of S-2-MeBA on this S-BrMBA site and therefore a calculated doping level of ~4% in the material (considering four types of S-BrMBA cations in the unit cell), which is consistent with the doping level of $3.9 \pm 1.4\%$ measured by solution NMR.

Notably, because of the expected low level of S-2-MeBA within the doped structures (and no heavy atoms in the dopant molecule), we do not expect to be able to detect/refine a well ordered and distinct set of sites for the dopant cation. On the other hand, the dopant may be reflected in the refinement parameters for the majority S-BrMBA cation sites. In this regard, we further analyzed the chemical occupancies of C and N atoms within the type B' S-BrMBA in the 3.9%

doping structure. In contrast to the low occupancy of 0.840 for the Br atom, a series of the C atoms (and the N atom) all show distinctly higher occupancy (> 0.95 on average, labeled in yellow in Supplementary Figure 4). The other two C atoms within the S-BrMBA cation (labeled in black in Supplementary Figure 4) show similar occupancy values as the Br atom. We hypothesize that this difference in the C atom occupancy may indicate that the C atom sites with high occupancy (> 0.95) are occupied by both S-BrMBA and S-2-MeBA; in contrast, the C atom sites with low occupancy are only occupied by S-BrMBA. Interestingly, we observe that the positions of the C atoms with high occupancies (> 0.95) roughly coincide with the molecular structure of S-2-MeBA (Supplementary Figure 4). It is noted that the C atom next to the Br atom is not expected to be part of S-2-MeBA; however, its chemical occupancy of 0.970 is close to 1, which we assume is due to the disorder of S-2-MeBA at this site. Such structural similarity leads to compatibility between S-BrMBA and S-2-MeBA in the doping process and may point to a reason why S-2-MeBA can be accommodated successfully within the (S-BrMBA)₂PbI₄ structure. Furthermore, we find that the ammonium groups of type A' and C' cations are located at similar positions relative to the inorganic lattice as indicated by their similar N – Pb/I distances (within ± 0.2 Å) (Supplementary Table 6 and Supplementary Figures 5-6), and correspondingly, the ammonium groups of type B' and D' cations are also located at similar positions (within ± 0.2 Å). We hypothesize that the relative position of the ammonium group of type B S-BrMBA is favorable for the S-2-MeBA substitution. Owing to the similarity between type B' and D' cations, there may also be a small amount of S-2-MeBA substitution at the type D' cation site, which leads to the slightly lower occupancy of Br (0.957) compared with type A' and C' cations. Thus, we here establish that one specific host cation site in the unit cell is preferentially occupied by dopant S-2-MeBA and the structural transition can only be driven when the proportion of the dopant reaches a critical level.

The doping variability within a single doping level batch was further considered by analyzing the chemical occupancies of an additional two 3.9% doping crystals, for which the occupancy values of type B Br atom show some range of values (i.e., 0.807 - 0.908; see Supplementary Table 7). NMR provides the average doping level (3.9 \pm 1.4%) for the entire sample batch and we expect to see a distribution (e.g., Gaussian) of the occupancy values among the crystals within the same batch. The determined doping levels observed for the three crystals fall within the compositional error reported for the NMR analysis. Additionally, the powder XRD

spectra of (S-BrMBA)₂PbI₄ and the 3.9% doping sample batches (Supplementary Figure 7) are consistent with their respective simulated XRD spectra (from the single crystal structures) and the distinct diffraction peaks between these two phases (changes in peak positions and intensities) indicate the impact of cation doping on the structures.

To investigate the possible impact of further doping level increase on the structure, we targeted materials with higher doping concentrations, by incorporating higher ratios of S-2-MeBA within the precursor solutions (see Methods). As for the previously discussed samples, the doping concentrations are evaluated through solution NMR (Supplementary Figure 8) and chemical occupancy analysis, yielding doping levels of $7.3 \pm 0.9\%$ and $7.8 \pm 1.5\%$ (subsequently labeled as "7.3% doping" and "7.8% doping" samples, respectively). Investigation of the 7.3% doping structure reveals lower chemical occupancy values for the Br atoms (Supplementary Table 7), indicating a higher doping concentration. This structure maintains the same P1 space group as the 3.9% doping phase, with slightly smaller lattice constants to accommodate the increased proportion of the smaller S-2-MeBA cation (Supplementary Table 1). Further analysis of the structural distortions in the 7.3% doping structure (Supplementary Table 8) indicates a comparable degree of distortions to the 3.9% doping phase. These findings suggest that a slightly higher doping concentration does not have a significant impact on the structural symmetry and distortions. Upon further increasing the doping level in the 7.8% doping phase, SC-XRD investigation reveals a new structure type ($P2_1$ space group) with larger superstructure (i.e., 65.699(2) Å along the b axis). We hypothesize that the higher concentration of S-2-MeBA leads to the rearrangement of organic cations, therefore contributing to the observed phase transition and adoption of a higher symmetry (relative to P1). Given the target of achieving lower symmetry in a well-ordered structure, our focus in this paper will be centered on the doping level range from 0% to 3.9% (i.e., the range of the first structural transition). The quality of the preliminary 7.8% doping level structure was not sufficient to establish the ordering of the organic cations and it is not further discussed.

Structural symmetry breaking in 2D HOIPs. To investigate the impact of chiral cation doping on structural symmetry, the space groups of the global and isolated inorganic structures were analyzed for each of the three structures with different degrees of S-2-MeBA doping (0%, 1.4%, and 3.9%). The (S-BrMBA)₂PbI₄ and the 1.4% doping structures adopt the same structure type and space group *C*2 (Supplementary Tables 1 and 2). However, upon further substitution, the 3.9%

Importantly, the space group of the isolated inorganic layer is also found to be P1 (Supplementary Table 2). The change of the global space group from C2 to P1 (individual inorganic layer: C2 and C2/m to P1) indicates that all existing symmetry elements (except for one-fold rotational symmetry) can be broken by a critical amount of S-2-MeBA doping and the associated structural transition. Notably, here we refer to the symmetry of the time and space-averaged structure. Clearly, on a local level, the introduction of a foreign cation will break the local symmetry in the immediate environment of that site. However, in the study of extended solid-state materials, many optical, electrical, and spin-related properties will rely on the time/space averaged structure, depending on the detailed scale of the fluctuations.

This symmetry breaking correlates with a rearrangement of organic cations (upon 3.9% S-2-MeBA doping). In (S-BrMBA)₂PbI₄ and the 1.4% doping structure, two subgroups of S-BrMBA (A, B and C, D) result in two types of inorganic layers. The corresponding cations are of the same type above and below the individual inorganic layers (Figure 3a-b). Such a symmetric arrangement leads to symmetric organic-inorganic interactions, which preserve the C_2 rotational symmetry axis within the inorganic sublattice along the b-direction (see Figure 3). To explore the different cation arrangements caused by 3.9% S-2-MeBA doping in detail, we further analyzed and compared the cation conformations between the (S-BrMBA)₂PbI₄ vs. 3.9% doping structures. Since the organicinorganic interactions mainly rely on the H-bonding between the ammonium groups and halogens, the relative N atom positions to the inorganic sublattice may impact the degree of strain introduced in the inorganic sublattice. Four types of organic cations possess four distinct relative N atom positions, due to the different conformations. As shown in Supplementary Figures 5-6 and Supplementary Table 6, we measured the distances between the N atoms and the adjacent Pb and I atoms within the puckered square pattern formed by four interconnected distorted PbI₆ octahedra, which are one set of parameters to describe the relative position of the N atom and distinguish the different conformations of the organic cations. By calculating the deviation of N – Pb/I distances between (S-BrMBA)₂PbI₄ and the 3.9% doping structures, we can rationalize designating type A', B', C', and D' cations in the 3.9% doping structure, in correspondence to type A, B, C, and D cations in (S-BrMBA)₂PbI₄, according to the arrangement that provides the lowest deviation among the N – Pb/I distances (on the level of $\sim 1\%$ or less). The radar charts of the N – Pb/I distances (Figure 4) further suggest that the ammonium groups of S-BrMBA cations mainly adopt two types of positions (i.e. A, C vs. B, D). The strong correspondence between the two structures indicates that the relative N atom position (ammonium group) of each single S-BrMBA cation is relatively stable and only subtly impacted by S-2-MeBA doping. As shown in Figure 3c, two distinct organic layers, consisting of one layer with an alternating arrangement of type A' and B' cations and the other layer with type C' and D' cations, interact with the single inorganic layer within the 3.9% doping unit cell (Figure 3c), wherein the symmetric arrangement of the organic cations is broken. From this analysis, we find that 3.9% S-2-MeBA doping promotes the subtle rearrangement of S-BrMBA cations, leading to a different structural symmetry (*P*1) and varying degrees of inter -and intra-octahedral distortions within the inorganic sublattice (Supplementary Table 8). In contrast, the difference in distortions between (S-BrMBA)₂PbI₄ and the 1.4% doping structure and between the 3.9% doping and the 7.3% doping structure is negligible, indicating that a significant impact on the global structural symmetry and distortions is primarily engendered by the doping induced structural transition.

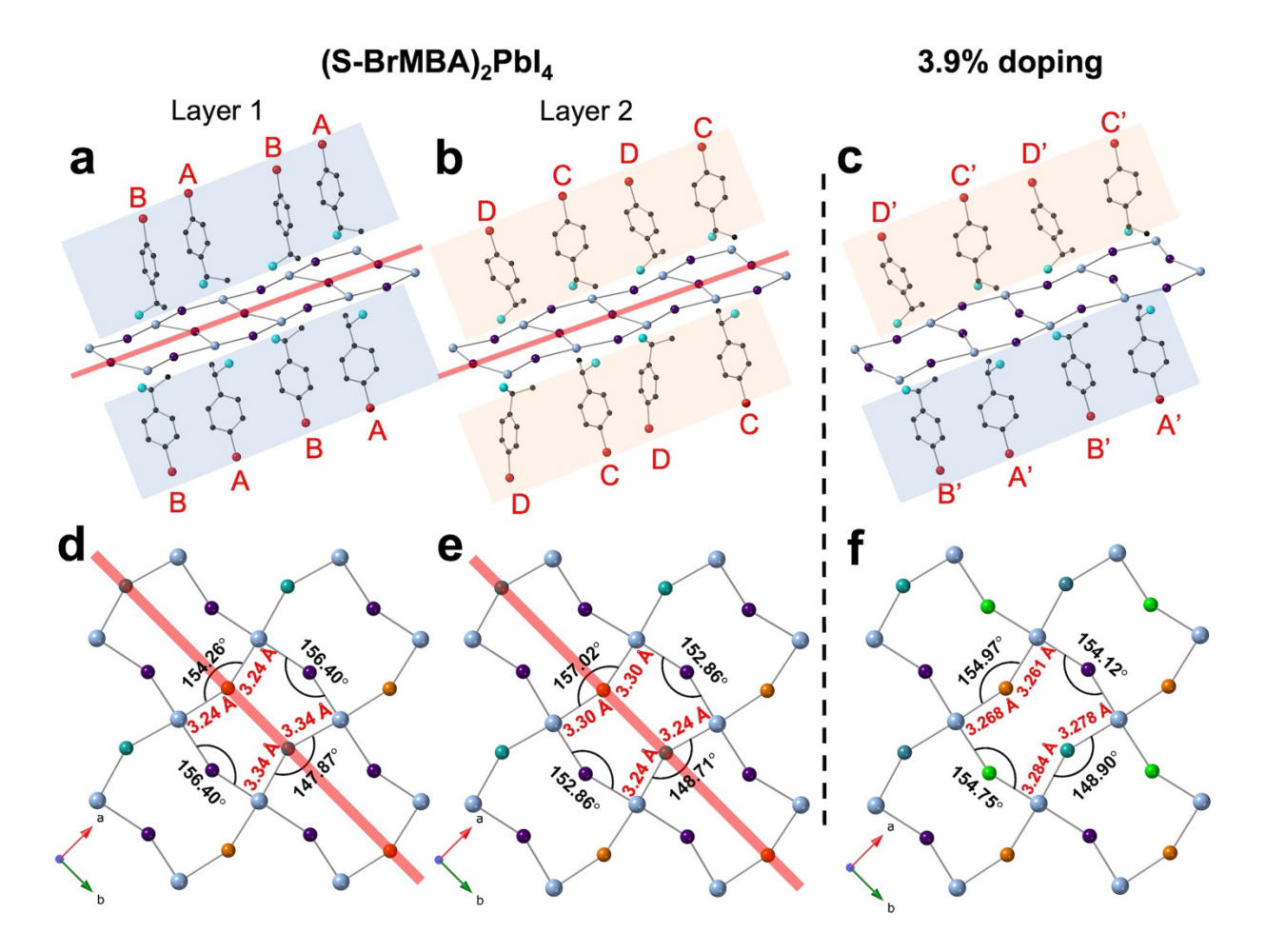


Fig. 3: a-c Arrangement and orientation of S-BrMBA chiral cations that bond to the inorganic layer 1 (a) and layer 2 (b) in (S-BrMBA)₂PbI₄, and the inorganic layer in the 3.9% doping structure (c). In (S-BrMBA)₂PbI₄, the two types of organic layers with alternating arrangements of A, B and C, D are highlighted by grey and tan shaded boxes, respectively. Grey, purple, red, black, and turquoise spheres denote Pb, I, Br, C, and N atoms, respectively. d-f, Schematic in-plane views of the inorganic layers corresponding to panels (a-c), respectively. Selected Pb-I-Pb bond angles and Pb-I bond lengths are labeled, indicating the two-fold (C_2) rotational symmetry within layer 1 and layer 2 in (S-BrMBA)₂PbI₄; in contrast, rotational symmetry breaking is noted in the 3.9% doping structure. The two-fold (C_2) rotational symmetry axes are represented by the red-shaded lines in layer 1 and layer 2. Axial I atoms are excluded in these images for visual clarity. In (S-BrMBA)₂PbI₄, grey, orange, blue-green, and purple spheres denote Pb, I(1), I(2), I(3) atoms in layer 1, and Pb, I(4), I(5), I(6) atoms in layer 2, respectively. In the 3.9% S-2-MeBA doping structure, blue, orange, blue-green, purple, and light green spheres denote Pb, I(1), I(2), I(3), and I(4) atoms, respectively.

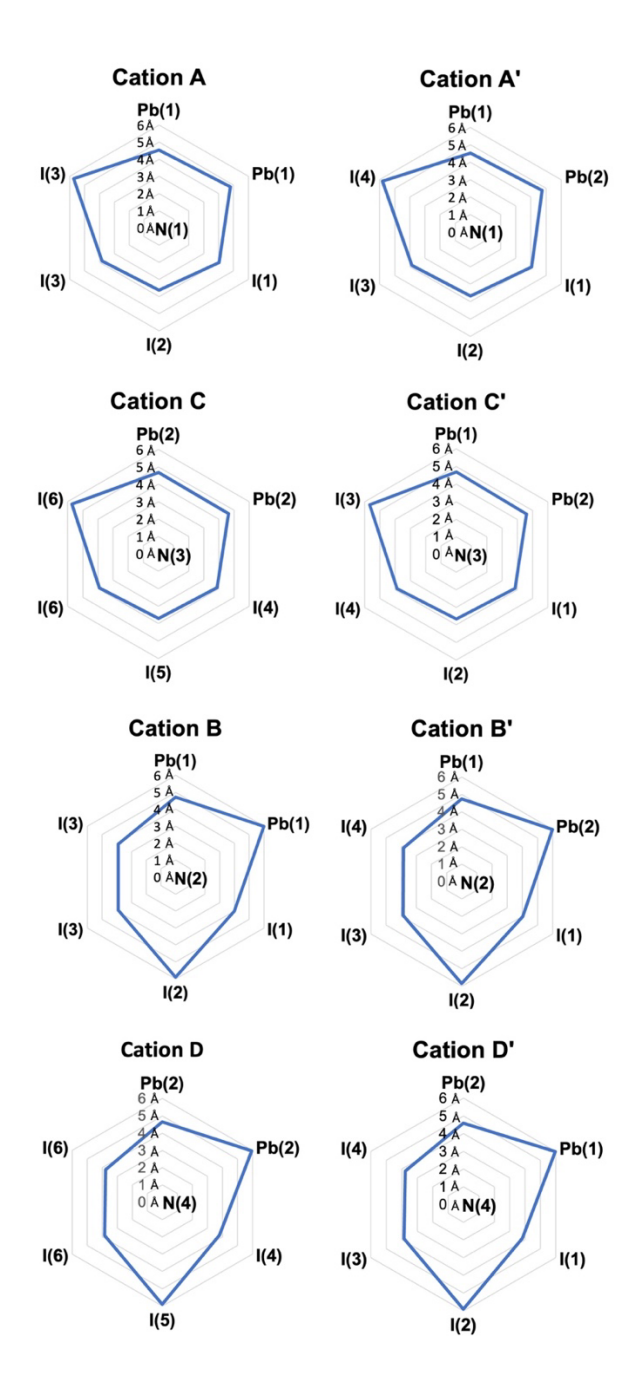


Fig. 4: Radar charts of the N-Pb/I distances of type A, B, C, and D cations in (S-BrMBA)₂PbI₄ and of the corresponding type A', B', C', and D' cations in the 3.9% doping structure. The detailed N-Pb/I distances are listed in Supplementary Table 6. The charts highlight the strong correspondence among A(A')/C(C') and B(B')/D(D') sets of cations in the two structures.

We further investigated the impact of organic-induced rotational symmetry breaking on the inorganic sublattice (distortion and symmetry) by analyzing changes in Pb and I atom positions upon doping. The fractional coordinates of Pb and I atoms of (S-BrMBA)₂PbI₄ and the 3.9% doping structure are listed in Supplementary Table 9. We aligned the axis choice and unit cell of the 3.9% doping structure with (S-BrMBA)₂PbI₄ for comparison (Supplementary Figure 9). In (S-BrMBA)₂PbI₄, two rotational symmetry axes, (0.5, 0, 0.5) and (0.5, 0, 0) (Figure 3d-e), are present in layer 1 and layer 2, respectively, based on atom I(1) and I(2) (layer 1) and I(6) and I(7) (layer 2) positions (Supplementary Table 9), coinciding with the C2 symmetry. In the 3.9% S-2-MeBA doping structure, Pb and I atoms deviate from their symmetric positions (Supplementary Table 9) and are no longer symmetric around (0.5, 0, 0.5), leading to the space group change from C2 to P1. Moreover, the deviation of Pb and I atoms further changes the Pb-I bond lengths and I-Pb-I bond angles. The symmetric bond lengths and angles across the C_2 rotation axis are preserved in layer 1 and layer 2 of (S-BrMBA)₂PbI₄ (Figure 3d-e). After 3.9% S-2-MeBA doping, these bond lengths and angles deviate from their symmetric values (Figure 3d-f), where an additional degree of distortion for breaking the rotational symmetry is engendered. Notably, within the puckered square pattern, the C2 rotational symmetry breaking leads to four types of independent I atoms, in contrast to the three types of I atoms in the single layer of (S-BrMBA)₂PbI₄ (Figure 3d-f). In summary, owing to the 3.9% S-2-MeBA cation doping, the structural-transition-induced asymmetric arrangement of S-BrMBA cations distorts the Pb and I atoms from their symmetric positions, which breaks the C2 rotational symmetry and lowers the single crystal structure (i.e., space/time averaged) space group symmetry to P1.

Spin-orbit Coupled Hybrid DFT Band Structure Calculations. To explore the effect of the doping induced structural transition on the electronic structure of the 2D HOIPs, we performed DFT calculations for the (S-BrMBA)₂PbI₄ and the 3.9% S-2-MeBA doping phase. The hybrid density functional HSE06³³⁻³⁴ with spin-orbit coupling³⁵ as implemented in the FHI-aims code³⁶⁻³⁷ was employed as further described in the Methods section. For the calculations reported in the main text of this work (Figure 5), the experimental structures obtained from SC-XRD were employed as the input data for investigating and comparing the electronic characters of the two phases, without any further structure optimization in DFT. The experimental structure for the 3.9% S-2-MeBA doping phase reflects a spatial average that does not include the local, site-specific structure changes surrounding a specific S-2-MeBA substitution. Also, the experimental unit cell

of the averaged 3.9% S-2-MeBA doping phase only contains eight molecules, i.e., a larger supercell model would have to be used to accommodate the concentration of 3.9% S-2-MeBA (which is below 12.5%, i.e., below one in eight molecules). However, even in such a larger model, the exact short-range order (if any) of the substituted S-2-MeBA molecules is not clear, and the Brillouin zones of the undoped and doped supercells would no longer be easily comparable. We therefore opted to employ the fixed, experimentally determined spatial average atomic positions of the 3.9% S-2-MeBA, to gauge the effect of the observed global symmetry breaking on the energy band structures. Importantly, for these fixed-geometry structures, we assume that each organic site is fully occupied by S-BrMBA, since no detailed S-2-MeBA atomic positions are available. However, the inorganic structural characteristics resulting from cation doping remain preserved. For comparison, structural relaxation was also attempted and the relaxed structures (although for a S-2-MeBA substitution of one in eight S-BrMBA molecules, i.e., a higher concentration than for the experimental structures studied) were used for additional electronic structure calculations, which are reported in detail in Supplementary Section S1 in the SI.

The calculated full band structures for the experimental atomic structures (Figure 5) indicate that the conduction band edges are derived from Pb states and valence band edges are derived from I states, which highlights the importance of the inorganic lattice (symmetry and distortions) in determining the electronic properties, especially the splitting of the conduction bands, i.e., spin splitting associated with inversion symmetry breaking in layered perovskites. We did not observe any significant participation of the Br component (part of the S-BrMBA molecules) in the frontier bands. To examine the splitting of the frontier bands, the conduction bands near the Γ point were recomputed with a 25-times denser sample grid along each k path. Note that the k-space paths shown in Figure 5a were chosen to be oriented in the directions of the plane defined by the real-space lattice vectors a and b (i.e., the inorganic plane), not the reciprocalspace directions a^* and b^* , which are not coplanar with the inorganic plane if the real-space c axis is not perpendicular to both real-space axes a and b. As shown in Figure 5b, (S-BrMBA)₂PbI₄ exhibits a Rashba/Dresselhaus-like spin splitting of $\Delta E=23.1$ meV (as defined in the caption of Figure 5) along the $\Gamma - X$ k-path and no such spin splitting along $\Gamma - Y$, as well as intermediate magnitudes of spin splitting along the diagonal $\Gamma - L$ and $\Gamma - K$ k-paths (14.3 meV). For the 3.9% doping phase, the band structure calculated using the experimental data shows a similar

Rashba/Dresselhaus-like spin splitting of ΔE =21.0 meV along the $\Gamma - X$ k-path and ΔE =0.3 meV along the $\Gamma - Y$ k-path (Figure 5b). Different from (S-BrMBA)₂PbI₄, the 3.9% doping phase exhibits different magnitudes of spin splitting (8.4 meV and 12.0 meV) along the diagonal $\Gamma - L$ and $\Gamma - K$ k-paths, associated with the rotational symmetry breaking within the inorganic sublattice. We note that the C2 rotational symmetry along the b axis does not, in itself, preclude spin splitting along the $\Gamma - Y$ path. This follows from the symmetry allowed spin Hamiltonian²⁸

$$H = b_{xx}S_xK_x + b_{yy}S_yK_y + b_{zx}S_zK_x$$

where S_x , S_y , S_z are spin operators and K_x and K_y are K vector components along the $\Gamma - X$ and $\Gamma - Y$ paths. Therefore, spin splitting is permitted along both the $\Gamma - X$ and the $\Gamma - Y$ paths. We surmise that the dominant term in the present structures is the b_{zx} term, which corresponds to R/D-like splitting, and that term is forbidden along the $\Gamma - Y$ path.

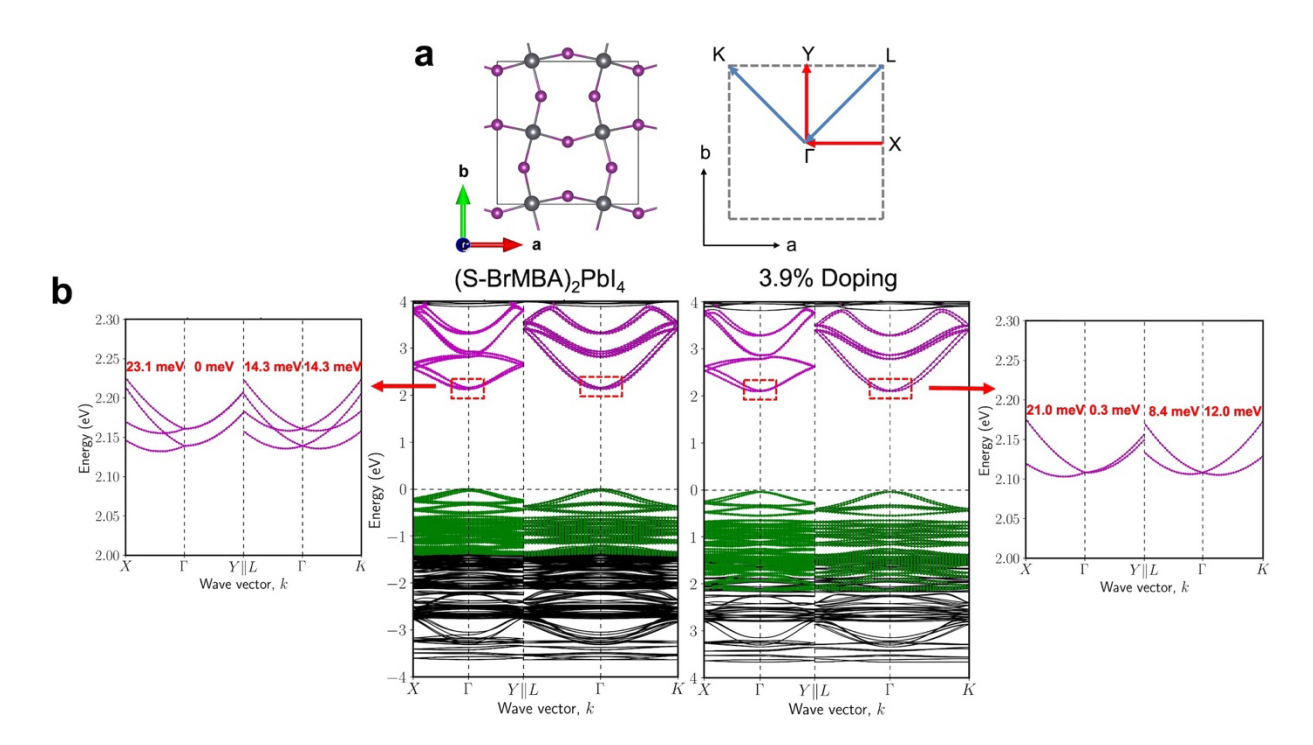


Fig. 5: DFT-based HSE06+SOC electronic band structure calculations for (S-BrMBA)₂PbI₄ and the 3.9% doping phase, completed using the experimentally determined lattice parameters and atomic positions. **a** Schematic of the real space unit cell (left) and the reciprocal unit cell (right) and the corresponding definition of the axis choice used for computational modeling, taking the (S-BrMBA)₂PbI₄ structure as an example. **b** Full band structures of (S-BrMBA)₂PbI₄ and the 3.9% doping phase. More finely resolved

calculations (relative to the full band structures) with 25 times denser sample grids are conducted to examine the spin splitting in the band structures along different k-paths, which are shown next to the full band structures. Spin splitting can be detected in the CBM of the two phases and the corresponding splitting magnitudes ΔE (the energy difference between the upper and lower conduction band branches at k_0 , which is the momentum where the lower band branch attains its minimum value) are labeled. Purple, green, and black colors denote Pb-, I-, and organic-derived electronic states, respectively.

Chiroptical properties. The impact of chiral cation doping and associated structural symmetry change on chiroptical properties was studied by measuring the circular dichroism (CD) of films of (S-BrMBA)₂PbI₄ and the 3.9% doping phase. CD is based on the diastereomeric interaction between chiral enantiomers with circularly polarized (CP) light³⁸, which is revealed by the differential absorption of left and right CP light. However, besides this intrinsic mechanism, the CD properties of anisotropic samples, including thin films in principle, can also originate from the interference of macroscopic anisotropies (linear dichroism (LD) and linear birefringence (LB))³⁸³⁹. According to the theoretical model based on the Mueller matrix analysis³⁸, the CD signal in anisotropic samples can be expressed by the following equation:

$$CD_{obs} \approx CD_{int} + \frac{1}{2}(LD' \cdot LB - LD \cdot LB') + (-LD\cos 2\theta + LD'\sin 2\theta)\sin \alpha$$
$$+ (P_x^2 - P_y^2)\sin 2\alpha (-LB\cos 2\theta + LB'\sin 2\theta),$$

where CD_{int} is the intrinsic CD component of the CD response of the anisotropic sample. The second term, $\frac{1}{2}(LD' \cdot LB - LD \cdot LB')$, accounts for the interference of macroscopic anisotropies, where LD and LB represent the linear dichroism and linear birefringence along x and y axes (perpendicular to the optical axis z); LD' and LB' are along the bisectors of the x-y axes (i.e., with a + 45° shift about the z-axis). The third and fourth terms are associated with a potential artifact that depends on the azimuthal angle θ , which indicates the angular orientation of the sample about the optical axis. These terms can be eliminated (if needed) by averaging the CD spectra over angle θ . Before comparing the CD properties and associating them with the structural symmetry, it is critical to demonstrate the origin of the CD signals—i.e. whether it is intrinsic, or whether it originates from the macroscopic LDLB effect or a combination of the two. One straightforward approach for confirming the presence of the LDLB effect is to flip over the sample, i.e. rotating by

180° around the x or y axes, and observe the difference in the CD spectra. The CD spectra will invert in sign or even yield a mirror profile if there is a sizable LDLB contribution. Otherwise, the CD spectra will be nominally consistent under these transformations and will reflect the intrinsic CD component CD_{int} in the equation above.

To examine the possible LDLB effect, the CD measurements in the current study were performed on the front and back sides of each film of (S-BrMBA)₂PbI₄ and 3.9% doping phase. The CD spectra measured on the front and back sides of each film are consistent, with only minor differences in peak magnitude (Supplementary Figure 12). This consistency suggests that the measured CD properties of (S-BrMBA)₂PbI₄ and the 3.9% doping phase are not due to the LDLB effect. However, in contrast to the 3.9% doping phase, which shows consistent CD spectra among different films, (S-BrMBA)₂PbI₄ shows distinct variation in CD peak intensities at the exciton energy among the different films (Supplementary Figure 12). To test whether such inconsistency relates to the artifacts from the instrument, such as the photomultiplier used as a planar polarizer that depends on azimuth angle (θ) , two representative films with distinct CD peak intensities at the exciton energy were selected and azimuth angle (θ) -dependent CD spectra were measured by performing the measurement after progressively rotating the films by 90°, coupled with front and back side measurement at each angle. As shown in Supplementary Figure 13, the CD spectra measured at different azimuth angles show similar profiles and peak shapes, with difference in the CD spectral magnitude, thereby indicating that the distinct peak shapes at the exciton energy do not arise from artifacts related to film orientation. Besides, we noticed that the difference in the CD spectral magnitude of film 2 (Supplementary Figure 13b) is obviously larger than film 1 (Supplementary Figure 13a) despite the two films having very similar absorbance. Considering the possible impact of film morphology on CD signals, we further performed SEM characterization for these (S-BrMBA)₂PbI₄ films. As shown in Supplementary Figure 14, pinholes were observed in some films; the presence of pinholes was found to be correlated with azimuthal-angledependence of the CD spectra and anomalous azimuthal angle dependent CD magnitude at the exciton energy, which could also be the reason for larger difference in the spectral magnitude at different azimuth angles of film 2 (Supplementary Figure 13b). Our observation preliminarily highlights the possible impact of morphological defects on detailed CD properties. In the future, a broader study is needed to further clarify the impact of film morphology on CD.

To compare the absorption, photoluminescence (PL), and CD spectra of (S-BrMBA)₂PbI₄ and the 3.9% doping phase, one representative film with good morphology (i.e., good uniformity and no large number of pinholes) was selected for each phase and the measured CD spectra were averaged over angle θ (Supplementary Figure 14-15). As shown in Supplementary Figure 16, (S-BrMBA)₂PbI₄ and the 3.9% doping phase show the same exciton peak position (centered at 2.50 eV), which is primarily associated with the electronic transitions from the valence band maximum (VBM) to the conduction band minimum (CBM)—i.e., states associated with the inorganic components of the hybrid. As noted by Du et al., the enlarged inter-octahedral distortion decreases both valence and conduction bandwidth and, thereby, increases the bandgap and associated exciton energy.³² Correspondingly, the 3.9% doping-induced subtle deviation of Pb and I atoms (Supplementary Table 9) leads to a similar degree of inter-octahedral distortion (Pb-I-Pb bond angle θ) between (S-BrMBA)₂PbI₄ (147.87°) and the 3.9% doping structure (148.90°), which contributes to similar exciton energy for the pure and mixed phases. As a result, an excitonic emission centered at 2.44 eV is observed for both phases (Supplementary Figure 16) in the photoluminescence (PL) spectra. Interestingly, the subtle structural symmetry and distortion change have an impact on the CD properties. As shown in Figure 6, (S-BrMBA)₂PbI₄ shows one first-derivative-featured CD band at the exciton energy. The corresponding CD band of the 3.9% doping phase shows polarity inversion relative to (S-BrMBA)₂PbI₄, which we associate with the change in the structural symmetry arising from the chiral cation doping. The polarity inversion of the 3.9% doping phase indicates that the cotton effect can be impacted by the chiral cation doping and the symmetry change. Moreover, we also found a ~45 meV blue shift of the center of the Cotton effect type line-shape (defined as the center between the two opposite peak points) of the 3.9% doping phase compared with that of (S-BrMBA)₂PbI₄. By normalizing the CD to the absorbance, we also can assess the dissymmetry spectra of the two phases (Supplementary Figure 17), where the highest dissymmetry values for (S-BrMBA)₂PbI₄ and the 3.9% doping phase are 1.79×10^{-4} and 1.88×10^{-4} , respectively. Our work indicates that the polarity and position of the CD band at exciton energy (associated with inorganic lattice) can be modulated by the chiral cation doping.

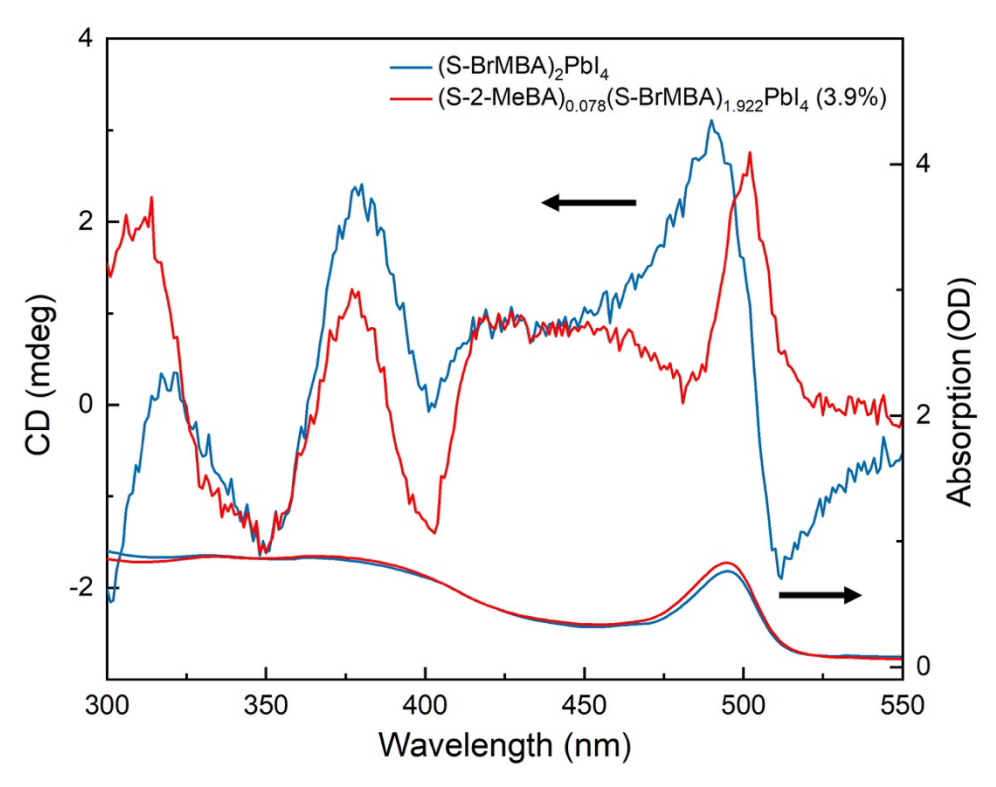


Fig. 6 CD spectra of (S-BrMBA)₂PbI₄ (blue) and the 3.9% doping phase (red). The corresponding absorption spectra are shown below. The term "OD" refers to optical density.

Thermal properties. Differential scanning calorimetry (DSC) was performed for (S-BrMBA)₂PbI₄, 1.4% doping, and 3.9% doping materials to examine the impact of cation doping on the thermal properties. The melting temperature, T_m , as demonstrated in the form of an endothermic peak upon heating in the DSC (and as verified by observing a sample on a temperature-controlled hot plate), decreases with an increase in the doping concentration (Figure 7). Notably, the lower T_m of the 1.4% doping (229.5 °C) compared to the (S-BrMBA)₂PbI₄ (231.6 °C) sample indicates a change of the thermal properties with doping, and this change appears despite a lack of structural transition to the lower symmetry phase. As the doping concentration further increases to 3.9%, the melting temperature lowers to 226.7 °C. Overall, we ascribe the lower melting temperature to the altered (more complex) organic steric effects and the associated organic-inorganic H-bonding interactions resulting from the re-packing of organic cations after S-2-MeBA doping. The degree of the melting temperature decrease is scaled with the doping concentration, pointing to the broader potential of suppressing T_m for 2D HOIPs via cation doping. In addition, the degradation points of the 1.4% doping and 3.9% doping materials, manifested as the broad exothermic peaks after the endothermic peaks in the DSC scans, occur earlier than that

of (S-BrMBA)₂PbI₄. We hypothesize that this reduced degradation temperature may relate to the enhanced ability of the lighter S-2-MeBA cation to leave the sample relative to S-BrMBA.

To further explore the degradation process, thermogravimetric analysis (TGA) was performed for these three materials (Supplementary Figure 18). The continuous weight decrease associated with the loss of organic components occurs from ~170 °C to ~250 °C, followed by the relatively stable solid residuals of PbI₂. The weight proportion of residual PbI₂ for the S-2-MeBA doping materials is theoretically higher than that of (S-BrMBA)₂PbI₄ due to the different formula weight (1115 g/mol for (S-BrMBA)₂PbI₄, 1112 g/mol for 1.4% doping material, and 1106 g/mol for 3.9% doping material). Indeed, we observe that the TGA curves for the 1.4% doping and 3.9% doping material are slightly higher than for (S-BrMBA)₂PbI₄ above ~250 °C, which agrees with the higher theoretical proportions of residual PbI₂ owing to the cation doping (expected: 0.4127 for (S-BrMBA)₂PbI₄, 0.4146 for 1.4% doping material, and 0.4167 for 3.9% doping material). We note that, in cases where hybrid perovskites are used for film/crystal melt processing, the loss of the organic components at the melting point can often be effectively prevented by employing a glass slide (or Kapton sheet) as a protective layer over the materials during the melting process.

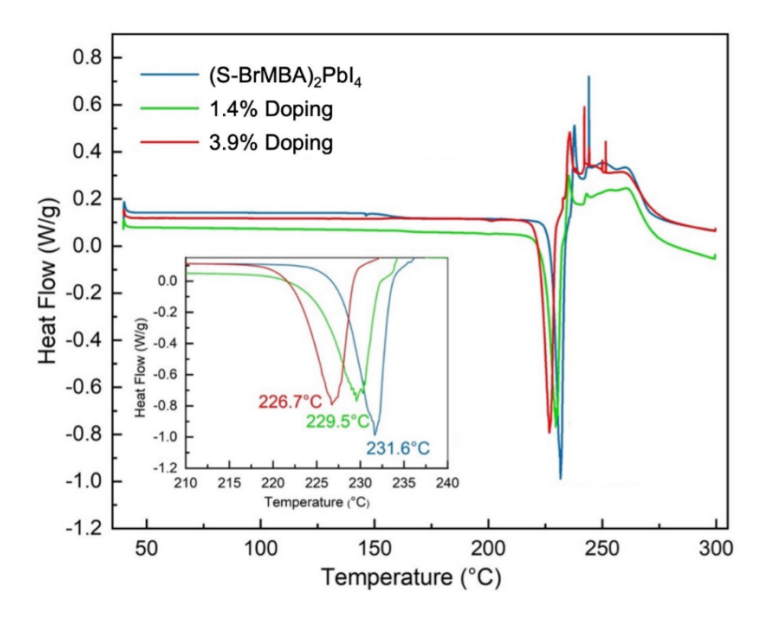


Fig. 7: Differential scanning calorimetry (DSC) scans of (S-BrMBA)₂PbI₄ (blue), 1.4% doping material (green), and 3.9% doping material (red) with the heating and cooling rate of 5 °C/min. The melting transition temperatures are labeled. The insert shows a zoom-in plot for the endothermic peaks corresponding to the melting transition.

Conclusions

In summary, we report low-level (<10%) chiral cation doping in a 2D HOIP. At a S-2-MeBA doping concentration level of ~4%, a rearrangement of BrMBA cations is facilitated and, as a result, the C_2 rotational symmetry in the organic layer is broken for the (S-BrMBA)₂PbI₄ pristine structure. The asymmetric arrangement of S-BrMBA cations shifts the Pb and I atoms from their original symmetric positions and induces an additional degree of asymmetric distortion into the inorganic structure. Therefore, the C_2 rotational symmetry within the inorganic sublattice is broken and the structure (global and isolated organic and inorganic sub-structures) transfers from a higher symmetry state (C2) to the lowest symmetry state (P1), which points to an extra degree of freedom in organic alloying to modulate structural distortions and symmetries. As a result, the spin splitting along different k-paths can be modulated, as corroborated by DFT calculations. The intrinsic chiroptical properties are also modified—i.e., the CD band corresponding to the exciton energy of the 3.9% doping phase shows polarity inversion and a ~45 meV blue shift relative to that for (S-BrMBA)₂PbI₄. Moreover, the cation doping effectively impacts the thermal properties—i.e., a higher doping concentration engenders lower melting temperature, which demonstrates the potential to suppress the melting transition of 2D HOIPs via cation doping. This, in turn, provides a crystal structure design paradigm toward even lower melting temperatures and holds promise for benefitting future film/crystal melt processing. 40 This controlled chiral cation doping and the associated doping-concentration-dependent structural transition manifests the potential for stabilizing novel 2D HOIP systems with a vast range of prospective combinations of mixed organic cations with flexible ratios (beyond 1:1) to finely modulate and enhance the emergent properties, in particular those that are sensitive to different types of symmetry breakings, and further benefit the development of emerging optoelectronic, magnetic, and spintronic technological advances.

Methods

Single Crystal Growth: All crystals studied in this paper were synthesized using the slow evaporation method. For (S-BrMBA)₂PbI₄, 0.125 mmol of PbI₂ and 0.25 mmol of organic amine (S-BrMBA) were dissolved into the mixed solvent of 2 mL aq. HI solution and 1.8 mL methanol. For 1.4% S-2-MeBA doping materials, 0.125 mmol of PbI₂, 0.188 mmol of organic amine (S-

BrMBA), and 0.062 mmol of organic amine (S-2-MeBA) were dissolved into the mixed solvent of 1.1 mL aq. HI solution and 1 mL methanol. For 3.9% S-2-MeBA doping materials, 0.125 mmol of PbI₂, 0.125 mmol of organic amine (S-BrMBA), and 0.125 mmol of organic amine (S-2-MeBA) were dissolved into the mixed solvent of 1.1 mL aq. HI solution and 1 mL methanol. For 7.3% S-2-MeBA doping materials, 0.125 mmol of PbI₂, 0.1 mmol of organic amine (S-BrMBA), and 0.15 mmol of organic amine (S-2-MeBA) were dissolved into the mixed solvent of 1.1 mL aq. HI solution and 1 mL methanol. For 7.8% S-2-MeBA doping materials, 0.125 mmol of PbI₂, 0.075 mmol of organic amine (S-BrMBA), and 0.175 mmol of organic amine (S-2-MeBA) were dissolved into the mixed solvent of 1.1 mL aq. HI solution and 1 mL methanol. These solutions were then kept in N₂ atmosphere. Slow evaporation of methanol over a one-week period yields yellow cubic crystals (Supplementary Figure 2a) of (S-BrMBA)₂PbI₄ and 1.4% S-2-MeBA doping materials, and yellow flaky crystals (Supplementary Figure 2b) of 3.9% doping, 7.3% doping, and 7.8% doping materials. The crystals were filtered and washed with ethyl ether and vacuum dried.

Thin-film deposition: Thin films of (S-BrMBA)₂PbI₄ and 3.9% S-2-MeBA doping phase were fabricated by dissolving the crystals in DMF solvent to achieve a 0.2 M solution and spin coating this solution on glass substrates (precleaned by ultrasonication in deionized water and IPA for 10 mins each, followed by Ar-O₂ plasma treatment for 10 mins) in an N₂ glove box. The spin coating recipe is 3000 rpm for 30 s followed by annealing at 100 °C for 10 mins.

Experimental characterization: ¹H NMR spectra were recorded on a Varian INOVA (800 MHz) spectrometer with cryogenic probe at room temperature. Samples were approximately 1 mM in concentration, including the S-2-MeBA and S-BrMBA standards purchased from Sigma Aldrich. All data were processed and analyzed using MNova (v 14.2.1) and 1 Hz line broadening. Chemical shifts are reported in ppm from tetramethylsilane (TMS) with the solvent resonance resulting from incomplete deuteration (DMSO: δ 2.47) as the internal reference. Data are reported as follows: chemical shift, multiplicity (s = singlet, d = doublet, t = triplet, dt = doublet of triplets, q = quartet, dq = doublet of quartets, m = multiplet), coupling constant(s) (Hz), and integration shape and value (Figure 2, Supplementary Figure 3, and Supplementary Figure 8).

Single-crystal X-ray diffraction (SC-XRD) characterization was performed on a Rigaku XtaLAB Synergy-S diffractometer using Mo K α radiation (λ =0.71073 Å) and operating at 50 kV

and 30 mA at room temperature (298K). Peak hunting, data reduction, and numerical absorption correction for all collected data were performed using CrysAlisPro. The crystal structures were solved and refined using SHELXS direct methods and SHELXL least-squares method within the Olex2 software package. During structure refinement, the chemical occupancies of targeted atoms are set as free. Symmetry analysis for each global structure and isolated inorganic structure (after deleting organic cations and, in the case of analyzing individual layers, the inorganic components associated with the other layer) was performed using PLATON's ADDSYM-EXT tool. The default angular tolerance factor is 0.3° for metric symmetry and the distance criterion is 0.25 Å for coinciding atoms for rotation, inversion, and translation symmetry elements. The positional/angular tolerance criteria were then changed to 0.2° (angular tolerance), 0.05 Å, 0.05 Å, 0.05 Å (distance criteria for rotation, inversion, and translation symmetry elements) for further symmetry analysis for each global structure and isolated inorganic structure.

Powder XRD analysis was performed for the powder samples using a PANalytical Empyrean powder X-ray diffractometer operating at 45 kV and 40 mA, with $CuK\alpha$ radiation. The powder samples were prepared by finely grinding the crystals on glass slides.

Differential scanning calorimetry (DSC) measurements were performed using a TA Discovery DSC instrument under nitrogen purge at a ramp rate of 5 K/min from 40 °C (313 K) to 300 °C (573 K). A hermetically sealed aluminum pan with lid was used to contain ~5 mg crystal for each sample. Owing to the decomposition of the hybrid perovskite during the high-temperature measurement, some bulging of the sealed sample pans was observed after the DSC scan.

Thermogravimetric analysis (TGA) measurements were performed on a TA Q50 instrument at a ramp rate of 1 °C/min from 25 °C (298 K) to 390 °C (663 K). A powder sample of ~5 mg was loaded for each measurement under nitrogen gas flow.

Regarding the room-temperature optical characterizations for the thin films of (S-BrMBA)₂PbI₄ and 3.9% S-2-MeBA doping phase, UV-Vis absorption spectra were characterized using a Shimadzu UV-3600i UV-Vis-NIR Spectrophotometer. The PL measurements were performed using a Horiba Jobin Yvon LabRam ARAMIS spectrophotometer, a 442 nm HeCd laser as excitation source, and an InGaAs detector. Circular dichroism (CD) measurement was performed on an AVIV 420 CD spectrophotometer with 1 nm/s scan speed.

First-principles calculations: The all-electron, full-potential electronic structure code package FHI-aims³⁶⁻³⁷ was used for all the first-principles simulations in this work. All band structure calculations are based on the Heyd–Scuseria–Ernzerhof (HSE06) hybrid functional³³⁻³⁴ and second-variational non-self-consistent spin-orbit coupling (SOC).³⁵ "Intermediate" numerical settings and associated atom-centered orbital (NAO) basis sets and a $(3 \times 3 \times 3)$ k point grid were used for the band structure calculations. In addition, the exploratory geometry optimizations reported in the SI are based on the Perdew–Burke–Ernzerhof (PBE)⁴¹ functional plus the Tkatchenko–Scheffler (TS)⁴² van der Waals correction, using "tight" numerical settings, associated NAO basis sets and a $(3 \times 3 \times 2)$ k point grid.

Associated Content

Supporting Information

Molecular structure of S-BrMBA and S-2-MeBA; photo of as-synthesized (S-BrMBA)₂PbI₄ and 3.9% doping crystals; ¹H NMR spectra of (S-2-MeBA)₂PbI₄ and (S-BrMBA)₂PbI₄; ¹H NMR spectra of $7.3 \pm 0.9\%$ doping and $7.8 \pm 1.5\%$ doping sample; Schematic of isolated type B' S-BrMBA cation with labeled chemical occupancies of C, N, and Br atoms, compared with the S-2-MeBA molecular structure; Schematic N-Pb/I distances and the radar chart of type A, B, C, D cations in (S-BrMBA)₂PbI₄ and the corresponding type A', B', C', D' cations in the 3.9% doping structure; Experimental and simulated powder XRD spectra of (S-BrMBA)₂PbI₄ and the 3.9% doping phase; Schematic unit cell transformation of the 3.9% doping structure; Structural relaxation and electronic structure calculations, including schematic in-plane views of inorganic layers of (S-BrMBA)₂PbI₄ and the 3.9% doping phase before and after DFT-PBE+TS relaxation, and DFT-based HSE06+SOC electronic band structure calculations for (S-BrMBA)₂PbI₄ and the 3.9% doping phase, completed using the DFT-PBE+TS relaxed lattice parameters and atomic positions; Measured CD spectra on the front and back side of (S-BrMBA)₂PbI₄ and 3.9% doping thin films; Azimuthal rotation angle (θ)-dependent CD spectra of (S-BrMBA)₂PbI₄ and the corresponding SEM images; Azimuthal rotation angle (θ)-dependent CD spectra of the 3.9% doping phase; Dissymmetry CD spectra of (S-BrMBA)₂PbI₄ and the 3.9% doping phase. roomtemperature UV-Vis linear absorption spectra and photoluminescence (PL) spectra for the (S-

BrMBA)₂PbI₄ and 3.9% doping phase films; thermogravimetric analysis (TGA) measurement results; single-crystal structural data, summary of structural symmetries, chemical occupancies of Br atoms, and structural distortion parameters of (S-BrMBA)₂PbI₄, 1.4% doping, 3.9% doping, and 7.3% doping phases; list of N – Pb/I distances and fractional coordinates of Pb and I atoms of (S-BrMBA)₂PbI₄ and the 3.9% doping phase; input geometries for all DFT calculations.

Accession Codes

The X-ray crystallographic data for this paper, namely, (S-BrMBA)₂PbI₄, (S-2-MeBA)_{0.028}(S-BrMBA)_{1.972}PbI₄ (1.4% doping), (S-2-MeBA)_{0.078}(S-BrMBA)_{1.922}PbI₄ (3.9% doping), and (S-2-MeBA)_{0.146}(S-BrMBA)_{1.854}PbI₄ (7.3% doping) have been deposited in The Cambridge Crystallographic Data Center (CCDC) database under deposition numbers 2261479, 2261482, 2261480, and 2278409 respectively. These data can be obtained free of charge via https://www.ccdc.cam.ac.uk/structures/ and also from the Hybrid³ perovskite database via https://materials.hybrid3.duke.edu/materials/search using the search terms: "(S-BrMBA)₂PbI₄", "(S-2-MeBA)_{0.028}(S-BrMBA)_{1.972}PbI₄ (1.4% doping)", "(S-2-MeBA)_{0.078}(S-BrMBA)_{1.922}PbI₄ (3.9% doping)", and (S-2-MeBA)_{0.146}(S-BrMBA)_{1.854}PbI₄ (7.3% doping).

Acknowledgment

This work was primarily supported as part of the Center for Hybrid Organic Inorganic Semiconductors for Energy (CHOISE) an Energy Frontier Research Center funded by the Office of Basic Energy Sciences, Office of Science within the U.S. Department of Energy. This research used resources of the National Energy Research Scientific Computing Center (NERSC), a U.S. Department of Energy (DOE) Office of Science User Facility operated under Contract no. DEAC02-05CH11231. This work was performed in part at the Duke University Shared Materials Instrumentation Facility (SMIF), a member of the North Carolina Research Triangle Nanotechnology Network (RTNN), which is supported by the National Science Foundation (award number ECCS-2025064) as part of the National Nanotechnology Coordinated Infrastructure (NNCI). The views expressed in the article do not necessarily represent the views of the DOE or the U.S. Government. The U.S. Government retains and the publisher, by accepting the article for publication, acknowledges that the U.S. Government retains a nonexclusive, paid-up, irrevocable, worldwide license to publish or reproduce the published form of this work or allow others to do

so, for U.S. Government purposes. Computational simulations by R.S. and J.M. were supported by NSF Award number DMR-1729297. N. A. M. S. C. assisted with computational simulations and gratefully acknowledges the financial support of FAPESP (São Paulo Research Foundation), grant number 20/11560-0, for his postdoctoral fellowship.

References

- 1. Mitzi, D. B. Synthesis, Structure, and Properties of Organic-Inorganic Perovskites and Related Materials. *Prog. Inorg. Chem.* **1999**, *48*, 1–121.
- 2. Saparov, B.; Mitzi, D. B. Organic-Inorganic Perovskites: Structural Versatility for Functional Materials Design. *Chem. Rev.* **2016**, *116*, 4558-4596.
- 3. Mao, L.; Stoumpos, C. C.; Kanatzidis, M. G. Two-Dimensional Hybrid Halide Perovskites: Principles and Promises. *J. Am. Chem. Soc.* **2018**, *141*, 1171-1190.
- 4. Mitzi, D. B. Templating and structural engineering in organic–inorganic perovskites. *J. Chem. Soc.*, *Dalton Trans.* **2001**, 1-12.
- 5. Jana, M. K.; Xie, Y.; Mitzi, D. B. Impact of Structural Distortions on the Optoelectronic and Spin-Related Properties of Two-Dimensional Hybrid Perovskites. In *Volume 1: Hybrid Organic Inorganic Perovskites: Physical Properties*, Beard, M. C., Ed. World Scientific Publishing Company, **2022**; Vol. *18*, 1-61.
- 6. Smith, M. D.; Connor, B. A.; Karunadasa, H. I. Tuning the Luminescence of Layered Halide Perovskites. *Chem. Rev.* **2019**, *119*, 3104-3139.
- 7. Mitzi, D. B.; Chondroudis, K.; Kagan, C. R. Organic-inorganic electronics. *IBM J. Res. Dev.* **2001**, *45*, 29–45.
- 8. Yang, C. K.; Chen, W. N.; Ding, Y. T.; Wang, J.; Rao, Y.; Liao, W. Q.; Tang, Y. Y.; Li, P. F.; Wang, Z. X.; Xiong, R. G. The First 2D Homochiral Lead Iodide Perovskite Ferroelectrics: [R- and S-1-(4-Chlorophenyl)ethylammonium]₂PbI₄. *Adv. Mater.* **2019**, *31*, 1808088.
- 9. Ai, Y.; Chen, X. G.; Shi, P. P.; Tang, Y. Y.; Li, P. F.; Liao, W. Q.; Xiong, R. G. Fluorine Substitution Induced High T_c of Enantiomeric Perovskite Ferroelectrics: (R)- and (S)-3-(Fluoropyrrolidinium)MnCl₃. *J. Am. Chem. Soc.* **2019**, *141*, 4474-4479.
- 10. Kepenekian, M.; Robles, R.; Katan, C.; Sapori, D.; Pedesseau, L.; Even, J. Rashba and Dresselhaus Effects in Hybrid OrganicInorganic Perovskites From Basics to Devices. *ACS Nano* **2015**, *12*, 11557–11567.
- 11. Long, G.; Jiang, C.; Sabatini, R.; Yang, Z.; Wei, M.; Quan, L. N.; Liang, Q.; Rasmita, A.; Askerka, M.; Walters, G.; Gong, X.; Xing, J.; Wen, X.; Quintero-Bermudez, R.; Yuan, H.; Xing, G.; Wang, X. R.; Song, D.; Voznyy, O.; Zhang, M.; Hoogland, S.; Gao, W.; Xiong, Q.; Sargent, E. H. Spin control in reduced-dimensional chiral perovskites. *Nat. Photonics* **2018**, *12*, 528-533.
- 12. Kim, Y.-H.; Zhai, Y.; Lu, H.; Pan, X.; Xiao, C.; Gaulding, E. A.; Harvey, S. P.; Berry, J. J.; Vardeny, Z. V.; Luther, J. M.; Beard, M. C. Chiral-induced spin selectivity enables a room-temperature spin light-emitting diode. *Science* **2021**, *371*, 1129-1133.
- 13. Abendroth, J. M.; Stemer, D. M.; Bloom, B. P.; Roy, P.; Naaman, R.; Waldeck, D. H.; Weiss, P. S.; Mondal, P. C. Spin Selectivity in Photoinduced Charge-Transfer Mediated by Chiral Molecules. *ACS Nano* **2019**, *13*, 4928-4946.
- 14. Wang, J.; Zhang, C.; Liu, H.; McLaughlin, R.; Zhai, Y.; Vardeny, S. R.; Liu, X.; McGill, S.; Semenov, D.; Guo, H.; Tsuchikawa, R.; Deshpande, V. V.; Sun, D.; Vardeny, Z. V. Spin-

- optoelectronic devices based on hybrid organic-inorganic trihalide perovskites. *Nat. Commun.* **2019,** *10*, 129.
- 15. Xu, Z.; Mitzi, D. B. SnI₄²-Based Hybrid Perovskites Templated by Multiple Organic Cations: Combining Organic Functionalities through Noncovalent Interactions. *Chem. Mater.* **2003**, *15*, 3632–3637.
- 16. Yan, L.; Jana, M. K.; Sercel, P. C.; Mitzi, D. B.; You, W. Alkyl-Aryl Cation Mixing in Chiral 2D Perovskites. *J. Am. Chem. Soc.* **2021**, *143*, 18114-18120.
- 17. Leung, T. L.; Tam, H. W.; Liu, F.; Lin, J.; Ng, A. M. C.; Chan, W. K.; Chen, W.; He, Z.; Lončarić, I.; Grisanti, L.; Ma, C.; Wong, K. S.; Lau, Y. S.; Zhu, F.; Skoko, Ž.; Popović, J.; Djurišić, A. B. Mixed Spacer Cation Stabilization of Blue-Emitting n = 2 Ruddlesden–Popper Organic–Inorganic Halide Perovskite Films. *Adv. Opt. Mater.* **2019**, *8*, 1901679.
- 18. Dresselhaus, G.; Kip, A. F.; Kittel, C. Spin-Orbit Interaction and the Effective Masses of Holes in Germanium. *Phys. Rev.* **1954**, *95*, 568-569.
- 19. Rashba, E. J. Properties of semiconductors with an extremum loop. 1. Cyclotron and combinational resonance in a magnetic field perpendicular to the plane of the loop. *Phys. Solid State* **1960**, *2*, 1224-1238.
- 20. Bychkov, Y. A.; Rashba, É. I. Properties of a 2D Electron Gas with Lifted Spectral Degeneracy. *JETP Lett.* **1984**, *39*, 78–81.
- 21. Du, L.; Hasan, T.; Castellanos-Gomez, A.; Liu, G. B.; Yao, Y.; Lau, C. N.; Sun, Z. Engineering symmetry breaking in 2D layered materials. *Nat. Rev. Phys.* **2021**, *3*, 193–206.
- 22. Xi, X.; Wang, Z.; Zhao, W.; Park, J.-H.; Law, K. T.; Berger, H.; Forró, L.; Shan, J.; Mak, K. F. Ising pairing in superconducting NbSe₂ atomic layers. *Nat. Physics* **2015**, *12*, 139-143.
- 23. Lu, J. M. Z., O.; Leermakers, I.; Yuan, N. F. Q.; Zeitler, U.; Law, K. T.; Ye, J. T. Evidence for two-dimensional Ising superconductivity in gated MoS₂. *Science* **2015**, *350*, 1353-1357.
- 24. Zhang, Y.; Holder, T.; Ishizuka, H.; de Juan, F.; Nagaosa, N.; Felser, C.; Yan, B. Switchable magnetic bulk photovoltaic effect in the two-dimensional magnet CrI₃. *Nat. Commun.* **2019**, *10*, 3783.
- 25. Ma, Q.; Xu, S. Y.; Shen, H.; MacNeill, D.; Fatemi, V.; Chang, T. R.; Mier Valdivia, A. M.; Wu, S.; Du, Z.; Hsu, C. H.; Fang, S.; Gibson, Q. D.; Watanabe, K.; Taniguchi, T.; Cava, R. J.; Kaxiras, E.; Lu, H. Z.; Lin, H.; Fu, L.; Gedik, N.; Jarillo-Herrero, P. Observation of the nonlinear Hall effect under time-reversal-symmetric conditions. *Nature* **2019**, *565*, 337-342.
- 26. Lee, J.; Wang, Z.; Xie, H.; Mak, K. F.; Shan, J. Valley magnetoelectricity in single-layer MoS₂. *Nat. Mater.* **2017**, *16*, 887-891.
- 27. Jana, M. K.; Song, R.; Liu, H.; Khanal, D. R.; Janke, S. M.; Zhao, R.; Liu, C.; Valy Vardeny, Z.; Blum, V.; Mitzi, D. B. Organic-to-inorganic structural chirality transfer in a 2D hybrid perovskite and impact on Rashba-Dresselhaus spin-orbit coupling. *Nat. Commun.* **2020**, *11*, 4699.
- 28. Jana, M. K.; Song, R.; Xie, Y.; Zhao, R.; Sercel, P. C.; Blum, V.; Mitzi, D. B. Structural descriptor for enhanced spin-splitting in 2D hybrid perovskites. *Nat. Commun.* **2021**, *12*, 4982.
- 29. Xu, Z.; Mitzi, D. B.; Dimitrakopoulos, C. D.; Maxcy, K. R. Semiconducting Perovskites $(2-XC_6H_4C_2H_4NH_3)_2SnI_4$ (X = F, Cl, Br): Steric Interaction between the Organic and Inorganic Layers. *Inorg. Chem.* **2003**, *42*, 2031–2039.
- 30. Schmitt, T.; Bourelle, S.; Tye, N.; Soavi, G.; Bond, A. D.; Feldmann, S.; Traore, B.; Katan, C.; Even, J.; Dutton, S. E.; Deschler, F. Control of Crystal Symmetry Breaking with Halogen-Substituted Benzylammonium in Layered Hybrid Metal-Halide Perovskites. *J. Am. Chem. Soc.* **2020**, *142*, 5060-5067.

- 31. Spek, A. L. Structure validation in chemical crystallography. *Acta Crystallogr.* **2009**, *D65*, 148-155.
- 32. Du, K. Z.; Tu, Q.; Zhang, X.; Han, Q.; Liu, J.; Zauscher, S.; Mitzi, D. B. Two-Dimensional Lead(II) Halide-Based Hybrid Perovskites Templated by Acene Alkylamines: Crystal Structures, Optical Properties, and Piezoelectricity. *Inorg. Chem.* **2017**, *56*, 9291-9302.
- 33. Heyd, J.; Scuseria, G. E.; Ernzerhof, M. Hybrid functionals based on a screened Coulomb potential. *J. Chem. Phys.* **2003**, *118*, 8207.
- 34. Heyd, J.; Scuseria, G. E.; Ernzerhof, M. Erratum: "Hybrid functionals based on a screened Coulomb potential". *J. Chem. Phys.* **2006**, *124*, 219906.
- 35. Huhn, W. P.; Blum, V. One-hundred-three compound band-structure benchmark of post-self-consistent spin-orbit coupling treatments in density functional theory. *Phys. Rev. Mater.* **2017**, *1*, 033803.
- 36. Blum, V.; Gehrke, R.; Hanke, F.; Havu, P.; Havu, V.; Ren, X.; Reuter, K.; Scheffler, M. Ab initio molecular simulations with numeric atom-centered orbitals. *Comput. Phys. Commun.* **2009**, *180*, 2175-2196.
- 37. Levchenko, S. V. R., X.; Wieferink, J.; Johanni, R.; Rinke, P.; Blum, V.; Scheffler, M. Hybrid functionals for large periodic systems in an all-electron, numeric atom-centered basis framework. *Comput. Phys. Commun.* **2015**, *192*, 60–69.
- 38. Albano, G.; Pescitelli, G.; Di Bari, L. Chiroptical Properties in Thin Films of pi-Conjugated Systems. *Chem. Rev.* **2020**, *120*, 10145-10243.
- 39. Zhang, Z.; Wang, Z.; Sung, H. H.; Williams, I. D.; Yu, Z. G.; Lu, H. Revealing the Intrinsic Chiroptical Activity in Chiral Metal-Halide Semiconductors. *J. Am. Chem. Soc.* **2022**, *144*, 22242–22250.
- 40. Singh, A.; Crace, E.; Xie, Y.; Mitzi, D. B. A two-dimensional lead-free hybrid perovskite semiconductor with reduced melting temperature. *Chem Commun (Camb)* **2023**, 59, 8302-8305.
- 41. Perdew, J. P.; Burke, K.; Ernzerhof, M. Generalized Gradient Approximation Made Simple. *Phys. Rev. Lett.* **1996,** 77, 3865-3868.
- 42. Tkatchenko, A.; Scheffler, M. Accurate molecular van der Waals interactions from groundstate electron density and free-atom reference data. *Phys. Rev. Lett.* **2009**, *102*, 073005.